MODELLING RAIL THERMAL DIFFERENTIALS
DUE TO BENDING AND DEFECTS

Chris BOSOMWORTH[1*], Maksym SPIRYAGIN[2#], Sanath ALAHAKOON[3], Colin COLE[4]

[1–4]Centre for Railway Engineering, Central Queensland University, Rockhampton, Australia
[1–4]Australasian Centre for Rail Innovation, Canberra, Australia

Abstract. Rail foot flaws have the potential to cause broken rails that can lead to derailment. This is not only an extremely costly issue for a rail operator in terms of damage to rolling stock, but has significant flow-on effects for network downtime and a safe working environment. In Australia, heavy haul operators run up to 42.5 t axle loads with trains in excess of 200 wagons and these long trains produce very large cyclic rail stresses. The early detection of foot flaws before a broken rail occurs is of high importance and there are currently no proven techniques for detecting rail foot flaws on trains at normal running speeds. This paper shall focus on the potential use of thermography as a detection technique and begin investigating the components of heat transfer in the rail to determine the viability of thermography for detecting rail foot flaws. The paper commences with an introduction to the sources of heat generation in the rail and modelling approaches for the effects of bending, natural environmental factors and transverse defects. It concludes with two theoretical case studies on heat generated due to these sources and discusses how they may inform the development of a practical thermography detection methodology.

Keywords: rail foot flaw, bending, temperature differential, modelling, heat transfer, thermography.

Notations

AEP – acoustic emission pulsing;
AET – acoustic emission testing;
EMAT – electromagnetic acoustic transducer;
IRT – infrared thermography;
LRUT – long range ultrasonic;
NDT – non-destructive testing;
RCF – rolling contact fatigue;
VSD – vehicle system dynamics.

Introduction

The heavy haul rail sector in Australia hauls approximately one billion tonnes of bulk product every year with the majority of that being iron ore. With gross wagon masses now reaching 170 t, significant deformation, wear, bending and shear stresses on the rail are the inevitable result. Combine this with the harsh natural environment that most rail operators work in and it is not surprising that defects and flaws occur in the rail (Spiryagin *et al.* 2014).

A review into condition monitoring for rail flaws (Papaelias *et al.* 2008) shows that rail head defects from RCF dominate the monitoring space, whilst techniques and research for rail foot flaw detection is limited. While it is no doubt understandable that head flaw detection is important, undetected foot flaws have caused derailments in Australia recently as detailed by the ATSB (2015) and the CI TS (2011). Rail foot flaws have also been cited by heavy haul rail operators in Australia as a risk to their safe and efficient operation.

There are two common types of rail foot flaws, longitudinal and transverse. Longitudinal foot flaws start as a vertical separation at the base of the web through the foot and travel longitudinally and outwards to the edge of the foot as shown in Figure 1 (Michaels 2014). They are caused by a number of different factors including segregations, inclusions, seams and improper bearing on ties or tie plates. These are currently only detected by visual observation and are sometimes called half-moon cracks. Transverse defects initiate at the edge of the foot caused by a nick or blow due to improper handling or usage of the rail. This type of flaw continues to grow transversely and, if left undetected, will result in a broken rail as shown in

Figure 2 (Michaels 2014). These are currently only detected by visual observation and are also called foot fractures (Michaels 2014; NSW Transport RailCorp 2012). This paper shall only focus on this type of rail foot flaw.

The foot flaw environment has constraints not seen in the rail head. Where the rail head is hopefully a smooth continuous surface, the foot has obstacles such as ties and fasteners as shown in Figure 3. This can make it problematic for contact, or near contact techniques, such as conventional ultrasonic (Krautkrämer, J., Krautkrämer, H. 1990), laser induced (Kenderian *et al.* 2006) or electromagnetic (Petcher *et al.* 2014) examination. Therefore, a non-contact technique may be the most suitable option for the detection of foot flaws. A brief review of existing detection techniques, contact, near contact and non-contact is presented in Section 1.

A potential method that to date has limited research in this area is IRT. It is a non-contact technique whose distance detection limitations are not as restrictive as the aforementioned techniques. There are two approaches for IRT, passive and active. The passive technique relies on the object under test in its natural state having defects at significant temperature differential to its surrounds, enabling direct detection. An example of this type of usage is human surveillance. The more common approach in practice is active IRT, where an excitation source is required to generate a heat flux in the object under test. The excitation generates a heat flux in the object and due to the higher thermal resistance of the defect or discontinuity a disturbance of the heat flux is generated creating a build-up of heat at the defect location that can be measured by an infrared camera (Maldague 2002).

For this reason, even though Thermography is a surface detection technique it is able to detect sub-surface faults as well. In this scenario, the heat energy build-up radiates in all directions away from the defect, and can be detected at the surface of the object. The development of a thermography based technique requires an understanding of the temperature differentials generated in the rail from rolling stock and whether additional excitation is required, or how the existing excitation can be leveraged for a detection technique.

The proposed foot flaw detection technique aims to install an infrared camera on a revenue raising rail vehicle, shown in Figure 4, travelling at speeds of up to 80 km/h. The preferred objective is to use an active Thermography technique, where the rolling stock provides the excitation to the rail. To establish the viability of the proposed method, a rail heat transfer model is being developed that is computationally fast enough to investigate complete heavy haul routes that may extend up to 500 km. For this reason, the modelling must be a reasonable approximation of what is occurring, without having the fine granularity that a more microscopic, computationally expensive, narrowed investigation might consider.

There are two research questions to be answered by this paper. Does bending due to rolling stock passage generate significant heat flux in the rail for use as an IRT active excitation technique, and further, does the change in flexural rigidity caused by a defect significantly impact the heat flux due to bending. This paper starts by describing the excitation sources provided by the contact of the rolling stock with the rail. It does not consider other external sources of thermal excitation such as lasers, induc-

Figure 1. Longitudinal foot flaw (half-moon defect)

Figure 2. Transverse defect (foot fracture)

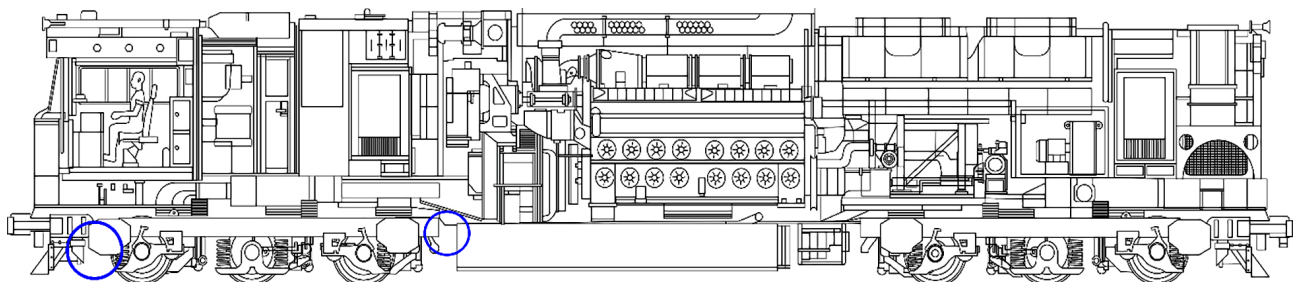Figure 3. Example of obstructions in the foot region

Figure 4. Proposed areas (blue circles) for installation of infrared camera for a thermography base detection technique

tive heating or heat lamps, typically associated with active Thermography. There is currently very limited research work in the area of rail heating due to rolling stock passage and thermography techniques for detecting rail foot flaws. A brief overview of the area is presented in Section 1.7. Therefore, this paper attempts to set the scene for current and future work in the area. Of the sources of heat identified, it looks specifically at bending and derives equations describing the generalised temperature differentials in the rail resulting from elastic hysteresis effects in the rail. The paper goes on to establish initial models integrating environmental effects such as convection and radiation and whether the change in flexural rigidity of the beam due to a flaw generates further heat due to bending.

1. Existing detection techniques

Review papers considering contact, near-contact and non-contact methods (Papaelias *et al.* 2008) and more recently by team member, Alahakoon *et al.* (2018), on non-destructive evaluation of rails presents a thorough state-of-the-art in defect technology. A summary of non-destructive techniques applicable to rail foot flaw detection from that time and recent advancements are shown in Table 1. A critique of the techniques follows, and will focus on the ability of the methods to detect rail foot flaws.

1.1. Ultrasonics

Ultrasonic inspection is classically a rail head detection technique. The transducers are water coupled to the rail and installed at differing detection angles to increase the probability of detection for defects (Krautkrämer, J., Krautkrämer H. 1990), refer to Figure 5. From the rail foot flaw context it is able to detect flaws in the base of the foot that are vertically below the rail head (ARTC 2019). This type of flaw is usually caused by corrosion and can be masked by any minor defects present vertically above it (Hernandez *et al.* 2007). As shown in the figure, it is unable to detect foot flaws that are initiated on the edge of the foot. Given obstructions such as rail fasteners and ballast foul-

ing, a coupled ultrasonic technique would be difficult to implement in practice.

1.2. EMAT

EMAT uses electromagnetic coupling between the transducer and the magnetic object under test to induce ultrasound waves. This is achieved by pulsing large current through an inductive coil positioned near a strong permanent magnet (Petcher *et al.* 2014). The use of EMAT is similar to conventional ultrasonic where it is mounted at different angles to the rail and is able to inspect a similar region (Figure 5). Although non-contact, the maximum lift-off distance between the inspection object and the base of the EMAT sensor is restricted to only several millimetres (Yi *et al.* 2010). From the rail foot perspective though, it is a closely coupled method in the order of millimetres, and would therefore pose practical implementation difficulties like the other contact or close contact methods.

1.3. LRUT

LRUT, also known as the ultrasonics guided waves technique, is based on the transmission of ultrasound as volumetric waves longitudinally in the rail. The configuration normally consists of piezoelectric transducers coupled to the rail and excited in the frequency range of 6 to 50 kHz
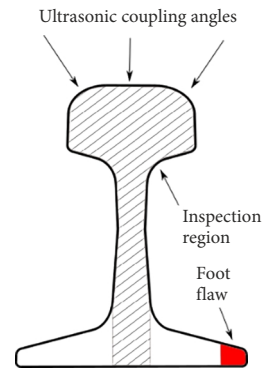

Figure 5. Conventional ultrasonics inspection region

Table 1. Defect detection techniques applicable to the rail foot

NDT technique	Systems available	Performance
Ultrasonics	manual and high speed system <19 m/s	»» may miss foot faults if other minor defects are present in web or head; »» manly able to scan central foot area directly below rail web
EMAT	low speed hi-rail vehicle <3 m/s	»» affected by lift-off variations; »» may miss some foot defects
LRUT	manual systems and low speed hi-rail vehicle systems <3 m/s	reliable in detecting transverse defects where overall cross section >5%
Laser ultrasonics	manual and low speed hi-rail vehicle systems <4 m/s	»» reliable in detecting internal defects; »» may be affected by lift-off variations with sensors
AEP	experimental	limited information – apparent similarities with laser ultrasonics for excitation and receiver
Vision systems		
Thermography	experimental	demonstrated for use in detecting RCF defects

(Bartoli *et al.* 2005; Hayashi *et al.* 2003). A coupled receiver measures the waveform and is analysed for reflections that can be localised and quantified. LRUT has been demonstrated in laboratory conditions to detect transverse defects at the outer edge of the rail foot (Campos-Castellanos *et al.* 2011; Moustakidis *et al.* 2014). However, from a moving vehicle detection perspective it has the same constraints as previously discussed methods, specifically coupling to the rail.

1.4. Laser ultrasonics

Laser ultrasonics is functionally similar to conventional ultrasound, however, uses laser pulses striking the sample to induce ultrasound in the rail as a non-contact generation source. The ultrasound waves are then received by an air coupled acoustic transducer. The advantage of this method is that both the laser and receiver can be place outside the danger zone of the rail foot environment making it useful for a higher speed moving vehicle technique. However, the distance from foot to acoustic receiver must be well controlled as it is susceptible to lift-off variation (Cerniglia *et al.* 2012; Green 2004; Kenderian *et al.* 2006; Scruby, Drain 1990).

1.5. AEP

AEP as a technique for rail flaw detection is in its infancy. It is conceptually similar to laser ultrasonics in that acoustic waves are injected into an object and recorded by an air coupled receiver. It is the active version of the common passive AET technique used in NDT (Grosse, Ohtsu 2008). It has been included in this review based on its similarities with laser ultrasonics only.

1.6. Vision systems

Machine vision systems capture high speed imagery of the track and its surrounds and post process the imagery through various techniques such as differential comparison (DelaCalle *et al.* 2017) and neural networks to detect features such as missing rail clips and rail surface flaws (Deutschl *et al.* 2004; Chen *et al.* 2010). As it is a non-contact method it is outside the danger zone of potential obstructions present in the foot area of the rail. The major drawback to the method is that it provides surface only detection, and hence any sub-surface flaws are not visible. No state-of-the-art or research work currently exists for using vision systems to detect rail foot flaws.

1.7. Thermography

There has been very limited research in the area of rail foot flaw detection using IRT. A paper by Greene *et al.* (2007) presented an experimental investigation into the use of differential Thermography for discerning transverse defects in the rail foot, however, the experiment ended up focusing more on head cracks then those in the foot. Of particular note, however, was the use of cyclic loading, or vertical wheel load, as excitation for the detection methodology. This contrasts with nearly all other techniques identified that use variations of electromagnetic excitation (eddy current heating) – Abidin *et al.* (2012), Peng *et al.* (2014), Tian *et al.* (2016), Wilson *et al.* (2011), Yang *et al.* (2015). However, Peng and Jones (2013) demonstrated the use of optical excitation and lock-in thermography for the detection of rail squats.

Although variations of eddy current thermography have shown particular promise in laboratory experiments, the heating and cooling times required for evaluation and detection pose some technical constraints for moving vehicles. In nearly all cases heating time ranged from 10 up to 200 ms (Wilson *et al.* 2011; Yang *et al.* 2015), with the cooling duration being in the seconds. Another issue related to the performance of eddy current heating is variations due to lift-off on moving vehicles, as the defect strength is inversely proportional to the cube of the lift-off distance (Papaelias *et al.* 2009).

2. Sources of heat

The development of a rail heat transfer model requires identifying the sources of heat either directly or indirectly generated by the rolling stock. Figure 6 outlines the different interactions between the wheel, rail and sleepers in a typical rail–sleeper configuration common in heavy haul networks worldwide. These interactions can be categorised into three areas – bending, wheel–rail contact and sleeper–rail contact. The fourth factor associated with rail heating, but not linked to rolling stock, are environmental factors such as solar and wind.

The key instigator for all dynamic interaction in the rail–rolling-stock setting and generation of heat is the wheel. Bending is the result of the normal and shear stresses in the rail caused by the pressure exerted by the wheel–rail contact as a result of vehicle body loading. Although an elastic event, the cyclic bending of the rail from each passing wheel causes a small temperature change in the rail steel due to the dissipated energy generated from internal molecular friction. The dissipated energy is a small proportion of the strain energy in the rail. While bending could be considered part of the wheel–rail contact process, for the purposes of this description it will be considered separately.
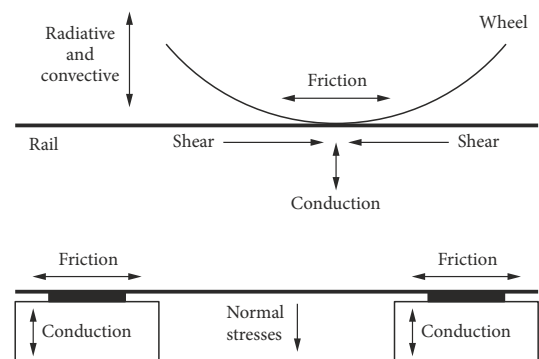

Figure 6. Sources of heat in a wheel–rail–sleeper interaction

Heat generation and transfer due to wheel–rail contact dynamics is a result of two processes, friction and conduction. The friction caused by the contacting surfaces can be very complex to model and is affected by external train handling factors such as traction, braking and VSD. Conduction is a result of the change in temperature between the rail and wheel. In a typical scenario, the wheel is at a higher temperature than the rail and their resulting interaction is known as rail chill.

The third dynamic effect is the sleeper–rail contact. In this case there is friction between the sleeper, or wear plate if one is present, and the rail that may result in a heating process in the underneath area of the foot. For concrete and steel sleepers, rail fasteners (or clips) are used to hold the rail in place unlike timber sleepers that employ the traditional rail spike. Conduction between the sleeper, wear plate and rail is particularly limited in the case of concrete and timber sleepers due to the insulating properties of sleeper materials. Steel sleepers nearly always employ some form of rubber/polymer wear pad that always insulates conduction between rail and sleeper.

The fourth heating process is quasi-static due to the natural environment. There is energy transfer through radiative and convective processes due to solar radiation, atmospheric conditions and the rail itself. These processes are affected by the rails' emissivity and angle of incidence of solar radiation and convection. For example, in early morning or late afternoon, only one side of each rail will be exposed to the sun; in the middle of the day, the top of rail and outer edges of the rail foot will be impacted. This will influence and change the way the rail is heated during the day.

The final heating process is by the foot flaw itself. There are two potential processes at work here, crack rubbing and crack growth. Under certain circumstances there will be internal frictional surface rubbing generating heat, although it is postulated that, in most cases, the crack will microscopically open and breath due to the shear force in the rail when the wheel rolls by. The last process is the tip itself undergoing plastic deformation as it grows, also generating highly concentrated heat in the tip.

3. Modelling approaches

Of the heat processes described, this paper shall focus on simplified approaches for modelling bending, environmental and crack defect effects. The other energy transfer processes such as wheel–rail contact and sleeper–rail contact shall be explored in greater depth in future work. As explained earlier the simplified approach is being adopted to enable simulation and evaluation of long heavy haul routes. The flowchart in Figure 7 outlines the general methodology that the paper will present.

3.1. Heat from bending

The first modelling approach to be evaluated is heat generated due to bending. As each wheel in a train rolls along the track there is a bending moment applied from the wheel-rail contact region. The length of the bending moment is dependent on the vertical stiffness of the sleeper and sub-track. Although the rail only undergoes elastic deformation during bending, there are internal frictional processes at the crystalline level due to non-homogeneities that dissipate heat. The effect of this is that a small proportion of the strain energy per bending cycle is converted to heat that may result in a change in temperature of the rail after many bending cycles. In modern heavy haul networks this may be anywhere between 400 to 1000 wheels per train in contact with the track.

The modelling approaches presented for bending shall consider the rail as a beam with the following assumptions:

»» the rail is fully insulated, i.e., no loss or gain of heat due to convection, conduction or radiation;

»» no frictional heat generated in the surface conditions by the application of the concentrated load, i.e., it is effectively a frictionless point mass;

»» the beam is uniform with no major defects, besides normal crystalline deformities, resulting in a small proportion of strain energy being converted to heat.

When a beam undergoes bending there is a tensile effect beneath the neutral axis and compressive effect above it. During elastic deformation, the tensile and compressive regions heat and cool respectively. When the beam returns to steady state, each region reverses in process and the beam returns to its original temperature, excluding the aforementioned internal friction and associated heat dissipation. The strain energy in a beam is a function of its bending moment and flexural rigidity as shown in Equation (1) (Jindal 2012). It describes the energy in the beam, i.e., it does not delineate between tension and compression, however it can be used in conjunction with the assumption of elastic strain hysteresis as a reasonable approximation of average temperature as a function of displacement in the beam due to bending.

The symbols for various parameters and their common values used throughout the remainder of the document
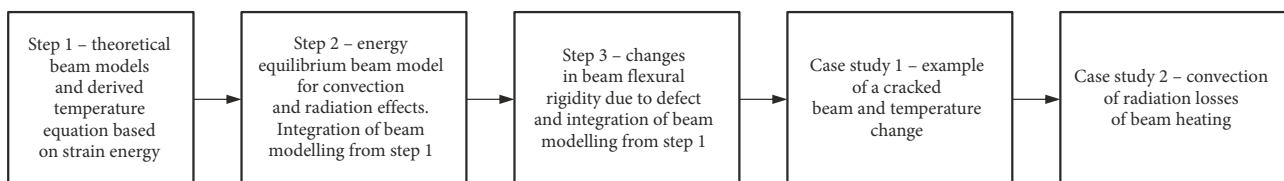
| Step 1 – theoretical beam models and derived temperature equation based on strain energy | Step 2 – energy equilibrium beam model for convection and radiation effects. Integration of beam modelling from step 1 | Step 3 – changes in beam flexural rigidity due to defect and integration of beam modelling from step 1 | Case study 1 – example of a cracked beam and temperature change | Case study 2 – convection of radiation losses of beam heating |

Figure 7. Outline of process presented by paper

are detailed in Table 2. The Young's modulus (Yu, Jeong 2012) and specific heat use the accepted value for steel. The second moment of inertia and 1 m length mass of rail are based on AS68 [kg/m] rail (Nippon Steel 2019). The concentrated load is equal to a single wheel load for a 42.5 t axle load and the beam length is equal to the standard sleeper spacing used by heavy haul rail networks.

$$U = \int \frac{M^2}{2 \cdot E \cdot I} dx. \tag{1}$$

Integrating for the total strain energy in the beam aggregates the energy function and resultant temperature information that is useful for understanding heating due to elastic hysteresis resulting from the bending moment. The integrand is a function of load and displacement, or the work done by the bending moment. The specific heat formula in Equation (2) can be used to generate a temperature function of displacement. If we consider a short length dx of the beam, the specific heat equation becomes Equation (3) and re-arranging for Δt the temperature function is Equation (4).

$$Q = m \cdot c \cdot \Delta t; \tag{2}$$

$$Q = Work(x) \cdot dx, \ m = m_{kg/m} \cdot dx; \tag{3}$$

$$\Delta t = \frac{Work}{m_{kg/m} \cdot c}. \tag{4}$$

3.1.1. Simply supported beam

The first approach considers the static problem of a simply supported beam with a concentrated load as shown in Figure 8 whose parameters are detailed in Table 3. In this method the sleepers are considered as infinitely stiff in the vertical direction, resulting in a bending moment that can at maximum be $l/2$. In practice this scenario is unlikely as the sub-track is never so stiff, however, as this is the shortest bending moment possible in sleeper-rail track configuration, it serves to inform on the minimum average temperature possible in the rail due to bending.

The strain energy integral in Equation (1) requires a continuous expression for the bending moment, resulting in separate work functions for sections AB (Equation (5)) and BC (Equation (6)). Substituting the bending moment of Equations (5) and (6) into Equation (1) produces in-

tegrals for solving the total strain energy in sections AB (Equation (7)) and BC (Equation (8)). Substituting the integrands from Equations (7) and (8) into Equation (4), our resultant temperature functions for sections AB and BC are shown in Equations (9) and (10). Equations (9) and (10) also introduce the proportional variable P_{int} that defines the component of strain energy that is dissipated as heat due to internal friction in the beam.

$$M_{AB} = \left(\frac{W \cdot b}{l} \right) \cdot x_{AB}; \tag{5}$$

$$M_{BC} = \left(\frac{W \cdot a}{l} \right) \cdot x_{BC}; \tag{6}$$

$$U_{AB} = \int_0^a \frac{W^2 \cdot b^2 \cdot x_{AB}^2}{2 \cdot E \cdot I \cdot l^2} \cdot dx_{AB}; \tag{7}$$

$$U_{BC} = \int_0^b \frac{W^2 \cdot a^2 \cdot x_{BC}^2}{2 \cdot E \cdot I \cdot l^2} \cdot dx_{BC}; \tag{8}$$

$$\Delta t_{AB}(x_{AB}) = P_{int} \cdot \frac{W^2 \cdot b^2 \cdot x_{AB}^2}{2 \cdot E \cdot I \cdot l^2 \cdot m_{kg/m} \cdot c}; \tag{9}$$

$$\Delta t_{BC}(x_{BC}) = P_{int} \cdot \frac{W^2 \cdot a^2 \cdot x_{BC}^2}{2 \cdot E \cdot I \cdot l^2 \cdot m_{kg/m} \cdot c}. \tag{10}$$

Temperature distributions for three different positions of the concentrated load on the simply supported beam are shown in Figure 9. Table 4 shows those three different position parameters. The average temperature generation in the beam for a single cycle is quite small, around $1.011 \cdot 10^{-4}$ K, however, extrapolating for many wheelsets, there is potential for a measurable accumulation of heat.
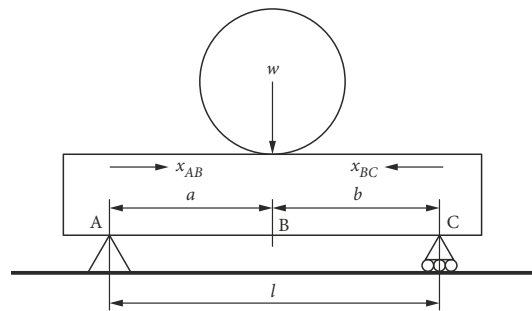

Figure 8. Vertical bending block diagram

Table 2. Temperature/strain parameters, symbols and common values

Symbol	Parameter	Unit	Value
U	total strain energy	J	
M	bending moment	N·m	
Δt	change in temperature	°C	
$Work$	work done	J	
E	Young's modulus	Pa	$2 \cdot 10^{11}$
I	second moment of inertia	m⁴	$3.94 \cdot 10^{-5}$
$m_{kg/m}$	mass of 1 m length of beam	kg	67.5
c	specific heat capacity	J/(kg·K)	450

Table 3. Additional simply supported beam parameters, symbols and values

Symbol	Parameter	Unit	Value
a	section AB distance	m	
b	section BC distance	m	
x_{AB}	dependant variable for section AB	m	
x_{BC}	dependant variable for section BC	m	
l	total length of beam	m	0.6
W	concentrated load	N	208462.5
P_{int}	proportion of strain dissipated as heat		0.05

Table 4. Concentrated load W positions for temperature distribution demonstration

Name	a [m]	b [m]
T1	0.1	0.5
T2	0.2	0.4
T3	0.225	0.375
T4	0.3	0.3
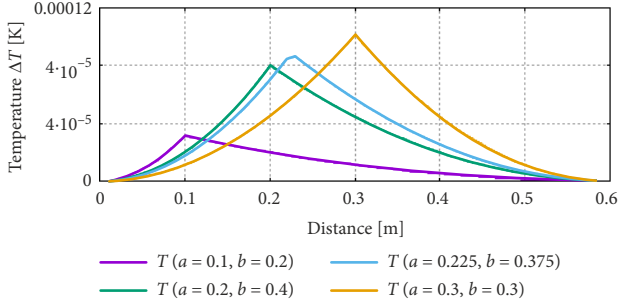
Figure 9. Change in temperature for a concentrated load on a beam

Wheel concentrated load W

Resultant bending for continuous elastic beam

Figure 10. Continuous elastic beam model

Table 5. Additional elastic beam parameters, symbols and values

Symbol	Parameter	Unit	Value
λ	damping factor		
k	track modulus	Pa	$20.7 \cdot 10^6$

Due to the infinite vertical stiffness of the end points of the beam, the maximum average temperature will occur in the middle of the beam, with no change in temperature at the end points as no bending ever occurs there.

3.1.2. Continuous elastic beam

The second approach considers a continuous elastic beam as described by Hay (1953) and shown in Figure 10. Unlike the simply supported beam whose coordinate system origin is located at the point of bending, this model's origin is at the point of maximum deflection in the beam. In the continuous elastic beam, the sleepers have a finite stiffness that is determined by the track modulus. This has a twofold effect, the length of the bending moment is significantly longer and all points on the track undergo the same maximum bending displacement for a constant wheel load as the wheels roll along. The resultant effect of this is that the track is uniformly heated. In practice this would not be entirely true as the effect of VSD may produce varying wheel loads on each of the wheelsets in the vehicle, and the track modulus is also not guaranteed to be consistent across an entire track network. To maintain consistency with the simply supported beam, we will assume 100% wheel loading, i.e., no under loading or overloading case due to VSD and constant track modulus.

The bending moment function is shown in Equation (11) and the new parameters introduced are detailed in Table 5. Like the simply supported beam, the moment function (Equation (11)) is substituted into the strain energy function (Equation (1)) that is substituted into (Equation (4)) to provide the temperature Equation (12). Substituting the bending moment function of Equation (11) into Equation (1) results in a work function:

$$M = W \cdot \left(\frac{E \cdot I}{64 \cdot k} \right)^{\frac{1}{4}} \cdot e^{-\lambda \cdot x} \cdot \left(\cos(\lambda \cdot x) - \sin(\lambda \cdot x) \right), \quad (11)$$
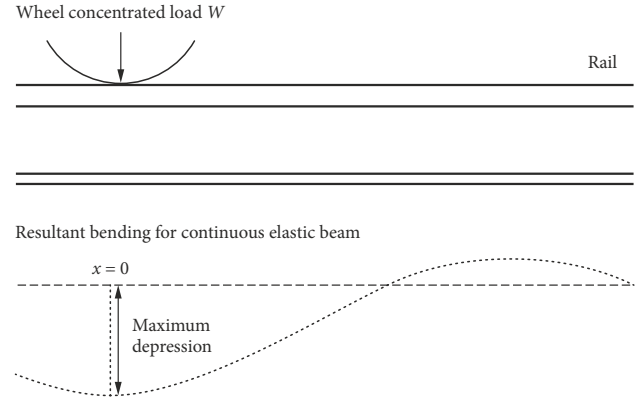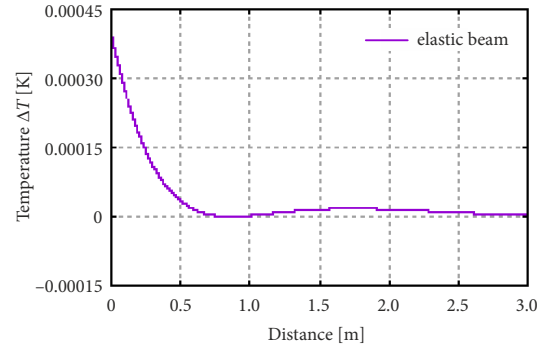

Figure 11. Continuous elastic beam temperature distribution

where:

$$\lambda = \left(\frac{k}{4 \cdot E \cdot I} \right)^{\frac{1}{4}};$$

$$\Delta t(x) = P_{int} \cdot \frac{f}{2 \cdot E \cdot I \cdot m_{kg/m} \cdot c}, \quad (12)$$

where:

$$f = \left(W \cdot \left(\frac{E \cdot I}{64 \cdot k} \right)^{\frac{1}{4}} e^{-\lambda \cdot x} \cdot \left(\cos(\lambda \cdot x) - \sin(\lambda \cdot x) \right) \right)^2.$$

This temperature distribution for the continuous elastic beam model is shown in Figure 11. The effect of the longer bending moment and subsequent increase in strain energy is quite clear with an average temperature in the beam at the point of maximum displacement being $4.0 \cdot 10^{-4}$ K. Like the simply supported beam, continuous wheelsets passing will potentially produce a cumulative temperature rise that will be discussed in greater detail later in the paper.

3.2. Heat from natural environment

The second approach to modelling presented by this paper is due to heat generated from the natural environment. As theoretical heat modelling shall be used to inform the development of a practical thermography based technique for a moving vehicle, it is important to understand the effect, if any, that weather will play in emissivity of the rail. The heating due to bending in the previous sections assumed no convection or radiation losses. The introduction of this model enables these energy loss components to be captured and will present a better representation of what average temperatures would be expected under practical conditions.

The patented work by Kesler, Zhang (2007) and Zhang, Lee (2008) details an energy equilibrium model for a beam floating in space. The model considers radiation, convection and stored energy of the rail and uses weather information (current and predicted), to calculate future track temperature. A block diagram of the model is shown in Figure 12 and its energy equilibrium relationship is expressed by Equation (13) for which the new parameters introduced are detailed in Table 6.
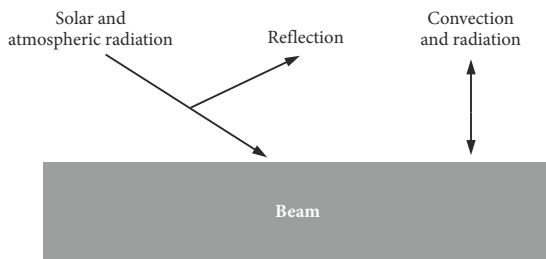

Figure 12. Transient heat transfer of a beam

Table 6. Energy equilibrium parameters and symbols

Symbol	Parameter	Unit
p	density	kg/m^3
c	specific heat capacity	J/(kg·K)
V	volume	m^3
T_r	rail temperature	K
k	atmospheric filtering factor	
α_s	solar absorptivity factor	
A_s	area of rail surface exposed to the sun	m^2
G_s	solar constant	W/m^2
θ	solar angle	°
h_{covn}	convection coefficient	
A_c	area of rail subject to convection	m^2
T_∞	ambient air temperature	K
ε	emissivity of rail	
σ	Stefan–Boltzmann constant	
A_r	area of rail subject to radiation heat transfer	m^2
T_{sky}	atmospheric sky temperature above cloud level	K
$\dot{E}_{other}$	term to account for heat exchange from rail–tie and rail–ballast	

$$\rho \cdot c \cdot V \cdot \frac{dT_r}{dt} = k \cdot \alpha_s \cdot A_s \cdot G_s \cdot \cos\theta -$$
$$h_{conv} \cdot A_c \cdot (T_r - T_\infty) +$$
$$\varepsilon \cdot \sigma \cdot A_r \cdot (T_t^4 - T_{sky}^4) + \dot{E}_{other}. \qquad (13)$$

To introduce the energy component generated by the internal friction, it is simply added through the E_{other} variable. The energy input is applied to the entire beam, therefore, to evaluate the beam under bending where the work done is a function of displacement, many beam slices are required to capture this effect. A case study is presented later in the paper to explore the heating effect of a train passage, demonstrating the premise and the role that environmental factors contribute. The energy component is added as a periodic impulse for each wheel.

3.3. Crack modelling

The introduction presented two types of rail foot defects that occur, longitudinal and transverse. This paper shall focus on transverse defects and present two approaches to modelling this type of defect through functions of varying flexural rigidity. The premise of this model is that a decrease in the flexural rigidity at the crack location will increase the strain energy at that point, due to the increase in bending, that in turn will produce a greater internal friction and resultant dissipated heat. The general observable phenomenon in the region would be a hot spot. This is not considering the plastic deformation that the crack tip itself generates or potential crack edge rubbing.

Both approximations assume the crack region is breathing, that is, the crack planes do not touch resulting in the flexural rigidity function not changing with time. This assumption is reasonable given the rail foot is under tension while there is a load applied from the wheel, therefore, for the majority of time it is open. The first approach by Christides and Barr (1984) approximates the crack region as an exponential function as shown in Equation (14):

$$EI(x) = \frac{E \cdot I_0}{1 + C \cdot e^{\frac{-2 \cdot \alpha \cdot |x - x_j|}{d}}}, \qquad (14)$$

where: $C = \dfrac{I_0 - I_c}{I_c}$;

I_0, I_c are the second moments of inertia for the undamaged and cracked sections of the beam respectively; d is the depth of the crack; x_j is the distance of the crack from the origin.

The α parameter can be used to control crack width. Examples of the function are shown in Figure 13, demonstrating two instantiations of the crack function with α configured as 0.667 and 4.0 respectively. For a standard beam, the inertia values can be calculated directly using the width and depth of the beam.

The second approach considers the crack as a triangular area. This is proposed by Sinha *et al.* (2002) as a
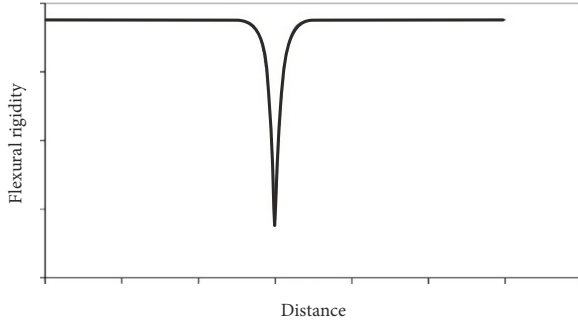
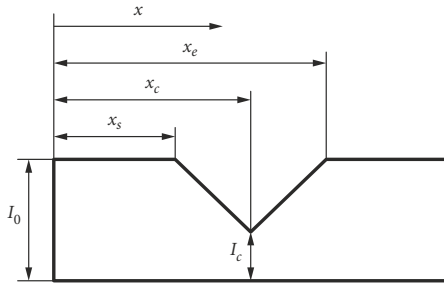Figure 13. Christides and Barr (1984) crack modelling using exponential function

Figure 14. Crack region modelling using a triangular section

Table 7. Additional parameters for vertical bending with crack model

Symbol	Parameter	Unit	Value
w	beam width	m	0.15
d	beam depth	m	0.1466
d_c	crack depth	m	0.01
I_c	crack inertia	m^4	$3.19 \cdot 10^{-5}$
x_j	crack centre from origin	m	0.0, 0.15, 0.30
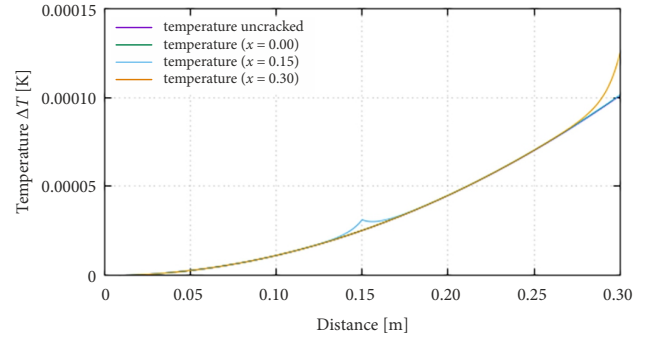
Figure 15. Change in temperature due to cracks and bending

simplification of the exponential function proposed in the first approach. The piece-wise linear functions for this crack model are shown in Equation (15) and the diagram in Figure 14. A benefit of this piece-wise approach is the ability to create asymmetry in the crack. To introduce crack flexural rigidity functions into the beam modelling only requires the constant EI to be replaced with the preferred $EI(x)$. Case study 1 presented in the next section demonstrates the average change in temperature around the crack region when applied to the beam model.

$$EI(x) = \begin{cases} f_1, \text{if } x_s \leq x \leq x_c; \\ f_2, \text{if } x_c \leq x \leq x_e, \end{cases} \qquad (15)$$

where:

$$f_1 = E \cdot I_0 - E \cdot (I_0 - I_c) \cdot \frac{x - x_s}{x_c - x_s};$$

$$f_2 = E \cdot I_0 - E \cdot (I_0 - I_c) \cdot \frac{x_e - x}{x_e - x_c}.$$

4. Case study 1 – vertical bending and cracking

This section shall investigate the effect of a crack on the average temperature generated in a rail due to vertical bending as a result of the change in flexural rigidity at the crack location. It shall use the equidistantly spaced concentrated load on a simply supported beam, with the Christides and Barr (1984) exponential crack model with the crack centre located at three different locations of section AB (Figure 7), namely $x_j = 0.0, 0.15$ and 0.30. All parameters required for this investigation are summarised in Table 7.

A H-beam rail approximation is selected as it has similar physical shape characteristics to those of rail. The crack model needs the second moment of inertia in x (I_{xx}) for

the un-cracked and cracked regions. AS68 rail (AS 1085.1-2002), used in heavy haul iron ore operations in Australia, has an approximate foot width w of 0.15 m and an I_{xx} of $3.94 \cdot 10^{-5}$ m^4. By rearranging the inertia Equation (16) for d, the depth of our H-beam approximation can be calculated. After substitution and solving, the depth of the beam is 0.1466 m and, in comparison, an AS68 rail is 0.17 m high, so it can be concluded that the approximation is a reasonable fit. To solve the inertia of the crack region, a crack depth must be selected. This has been arbitrarily chosen as 0.01 m based on qualitative observations from Figures 1 and 2. Further sensitivity around the crack depth may be the topic of future work. The relationship for solving the inertia of the crack is shown in Equation (17) and solving for the crack inertia results in a value of $3.19 \cdot 10^{-5}$ m^4.

$$d = \sqrt[3]{\frac{12 \cdot I_c}{w}}; \qquad (16)$$

$$I_c = \frac{w \cdot (d - d_c)^3}{12}. \qquad (17)$$

Figure 15 shows the change in temperature for the three different crack locations tested. It can be seen that, as the crack is located further from the origin, the resultant temperature rise increases significantly. This is as a result of the squared complexity of the functions in Equations (9) and (10) and the reduction in flexural rigidity at the crack centre. At its largest the average temperature at the crack region is $1.252 \cdot 10^{-4}$ K, which is a 23.9% higher temperature than just the temperature change due to un-cracked bending.

The result for the simply supported beam raises some interesting questions for a thermography based detection

algorithm as it demonstrates that, for the same crack in different locations, the temperature differential is significantly different. While it's been discussed that sleepers are not infinitely stiff in practice, it should be noted that sleepers are also not all equivalent stiffness. This is important when attempting to quantify the severity of the crack, or in the worst case, even seeing the crack at all. In the case where the crack is located close to the support, there is no temperature differential due to bending generated at all and a thermography based technique will need to rely on another form of excitation to identify the presence of a crack in this case.

5. Case study 2 – bending and environment

The final case study investigates the cooling effect of the environmental model undergoing bending. It considers the time-series problem of a train with many wheel loading impulses. Meta-data for the simulation is shown in Table 8. The parameters have been derived for a 250 wagon train with approximately 1000 wheels per left and right rail. This long train configuration is common for Heavy Haul iron ore operators in Australia. Each wagon is comprised of two three-piece bogies with 2 wheelsets per bogie. Due to the density of iron ore, the wagon lengths are shorter than typical freight wagons and are only 10…12 m long resulting in a train length of 3000 m. The wheel spacings are averaged based on this length and number of wheels on each side of the train. In practice the wheelset spacing per bogie, wagon and inter-wagon are irregular, however, an average approximation is considered reasonable for this analysis. The train speed of 15 m/s is reasonable for heavy haul operations with typical trip speeds varying between 11.11 and 22.22 m/s.

As described in Section 3.2, the rail must be split into many finite slices to capture the change in energy over time of the internal friction work done in the rail. Table 9 shows the beam parameters. The beam length has been selected based on standard sleeper spacing, whilst the rail parameters, circumference, surface area and mass are all calculated from AS68 rail standards.

The environmental energy equilibrium function in Equation (14) is simplified to remove the effect of solar radiation and atmospheric black body radiation, and only considers the radiation of its surrounds. This simplification is justified in that, during train passage, neither solar nor black body radiation will be applied to the rail as the train itself physically restricts both these phenomena. Given the intention of mounting the instrumentation on the train, what happens after the train has passed is not applicable to the problem. The resulting differential relationship is shown in Equation (18). The specific heat assumes a standard value for steel whilst the surface areas for convection and radiation are calculated for the rail slice and assume that the longitudinal ends and foot of the slice are not exposed to either radiation or convection. In practice the longitudinal ends would only be subject to convection. The emissivity is based on rusted steel that varies between 0.75 and 0.85. The polished running band of the

rail, which has low emissivity has not been considered and is small in comparison to the remaining surface area.

$$\rho \cdot c \cdot V \cdot \frac{dT_r}{dt} = h_{conv} \cdot A_c \cdot \left(T_r - T_\infty \right) +$$

$$\varepsilon \cdot \sigma \cdot A_r \cdot \left(T_r^4 - T_\infty^4 \right) + \dot{E}_{other} . \tag{18}$$

A comparison of the resultant temperature of the beam both with and without the environmental model is shown in Table 11. In this particular scenario the loss of energy in the beams slices is very low in comparison to the theoretical case where no environmental model is applied. Given the small change in temperature, the radiation and convection components are extremely small for all coefficient of cooling parameters selected. Obviously, for a larger temperature differential between rail and ambient, there will be a faster cooling effect given the inverse exponential function.

Table 8. Meta-data for time-series bending and environmental model

Parameter	Unit	Value
Train length	m	3000
Number of wheels (left or right rail)		1000
Average wheel spacing	m	3
Train speed	m/s	15
Time between wheel loads	s	0.2
Convection coefficient		10

Table 9. Parameters for the beam model

Parameter	Unit	Value
Beam length	m	0.6
Number of slices		100
Slice width	m	0.006
AS68 circumference	m	0.67
Slice surface area	m²	0.0042
Slice mass	kg	0.408

Table 10. Values for the environmental model

Symbol	Parameter	Unit	Value
c	Specific heat capacity	J/(kg·K)	450
T_r	rail temperature	K	
h_{conv}	convection coefficient		0, 10, 20, 30
A_c	area of rail subject to convection	m²	0.0042
T_∞	ambient air temperature	K	303
ε	emissivity of rail		0.75
σ	Stefan–Boltzmann constant		$5.67031 \cdot 10^{-8}$
A_r	area of rail subject to radiation heat transfer	m²	0.0042
$\dot{E}_{other}$	a term to account for heat exchange from rail-tie and rail-ballast		0

Table 11. Resultant beam temperature after train and environmental model

Convection coefficient	Max temperature [K]
0	303.101375
10	303.101204
20	303.101089
30	303.100974

6. Discussion

To use thermography for rail foot flaw detection requires that sufficient temperature differential can be generated around the source of the defect. This heat flux across the higher resistance of the crack is what generates localised heat spots detectable by Infrared. Readily available commercial uncooled micro bolometer type infrared sensors have temperature sensitivities of < 0.06 K (FLIR 2016) so theoretically the temperature differential requirements are quite low. In practise, the variations in emissivity on the rail foot due to contamination or corrosion will elevate the temperature differential noise floor requirement for positively identifying a flaw in the region. A practical evaluation of this noise floor value has yet to be studied in detail.

Figure 9 shows that, for the simply supported beam model the change in average temperature at the maximum bending displacement for a single cycle is approximately $1.011 \cdot 10^{-4}$ K and occurs when the concentrated load is equidistantly spaced between the two supporting ends of the beam that are vertically infinitely stiff. In contrast, the model in Section 3.1.2 assumes a beam that is a continuously supported elastic beam. Its bending moment function is derived based on knowledge of the rail, sleeper and ballast track structure. Figure 10 shows the maximum temperature at the maximum deflection point is $4.0 \cdot 10^{-4}$ K, which is nearly 4 times greater than for the simply supported beam model. This is not unexpected given the strain energy has squared complexity and the point of bending begins much further away in the continuous elastic beam model. This result provides some useful knowledge of expectations of sensitivity of heat dissipation in the rail due to bending.

Case study 1 investigated the changes in heat due to bending by varying the flexural rigidity in the rail as a result of a crack. A H-beam was chosen due to its similarity to rail and parameters calculated to match the inertia in the longitudinal direction of an AS68 piece of rail. A 10 mm transverse crack was assumed and the modified flexural rigidity calculated. Applying the simply supported beam model demonstrated an increase in temperature at the maximum displacement point of just under 24% with a crack present, and, taking into account the conservatism of this approach, the percentage will be higher for a longer bending moment such as that used in the continuous elastic model. Laboratory validation and further work is required to determine if this approach is reasonable as practical characterisation of a rail foot flaw.

Although the individual temperature rise in both beam models are well below the sensitivities of commercial infrared sensors, case study 2 quantifies the effect of a train passage for a modern heavy haul train. Table 11 shows the effect of multiple wheel loads of excitation using the simply supported beam model with the convection and radiation environmental effects introduced in Section 3.2. In the theoretical case, a 250 wagons train with approximately 1000 wheels travelling at 15 m/s would create a temperature rise of 100 mK in the rail. This small rise resulted in very little influence from environmental effects. Noting that the simply supported beam produced about 4 times less average temperature in the rail then the continuous elastic model, we can assume that the change in temperature may be as high as 400 mK for this scenario.

The results presented have all assumed a constant wheel load and therefore do not take into account the effect of VSD. In a tangent running case, the assumption of a static wheel load is reasonable for normal operation without significant track irregularities and defects. In the case of track defects and irregularities, there may be localised areas of moderate to large changes in wheel load that may significantly influence heat generation. For the curving cases, it is common in heavy haul train operations that trains run in a cant deficient state. Cant is defined as the change in vertical elevation between the high and low rail in a curve. The result of cant deficiency is that the high rail is under greater load than the low rail. The result of this in the context of bending is the high rail would have larger bending moments than the low rail and larger internal temperature generation. The models presented can be incorporated into multibody simulation to evaluate this effect, which is planned for future work.

For the proposed problem of detection of rail foot flaws from a moving vehicle using rolling stock excitation, it has been discussed that there is a heat energy component present due to bending that will vary according to the state of the train. What is clear is that bending by itself in small numbers of cycles, or individual cycles, will not be measurable by conventional uncooled micro bolometers, however, for large heavy haul trains with many wheelsets, there is a measurable change in rail temperature. Considering bending in isolation, it is clear that the most appropriate location for installation of the Infrared camera is at the rear of the train to optimise the heating potential. Future work needs to consider the heat flux in the rail and also how it interacts with the crack, as the current models only consider the average temperature at a location in the beam.

The results thus far do demonstrate that thermography may be a suitable methodology for the detection of rail foot flaws. With other sources of heat such as friction and conduction to be considered, and further exploration around crack self heating, the number of vehicles required for excitation capable of generating suitable temperature differentiation is hoped to drop considerably.

Conclusions

This paper commenced by describing the proposed method of moving vehicle rail foot flaw detection via a thermographic method. The method aims to use the rolling stock as excitation for rail heating, and the paper presented the different sources possible through this interface. The main focus of the paper then concentrated on heating due to bending, with the authors deriving equations based on bending strain energy in a beam and specific heat, in conjunction with elastic hysteresis to quantify the resultant energy and temperature differential. An existing energy equilibrium beam model capturing environmental effects such as radiation and convection was presented and the authors presented how this could be integrated with the derived beam energy equations to enable a more practically informative analysis. The modelling concluded with the presentation of existing work on flexural rigidity change due to a crack in a beam and how this could also be considered in the beam modelling.

Two case studies were presented, the first of which used the crack and bending model to investigate the changes in heat generated by the crack for different locations of the wheel load along the simply supported beam. The key lesson learnt from the case study is that while the simply supported beam may not be practically representative it did raise an interesting question that in practice the bending moment of the rail is not guaranteed to be constant and therefore the strain energy may change significantly, resulting in different temperature changes for the same crack. This is an important consideration for all heating processes in future work, and attempted characterisation of defects.

The second example considered the effect of whole of train wheel load excitation on temperature in the rail and the amount of energy lost due to environmental factors. It was shown that the temperature rise under the constant conditions of the simulation may result in a rail heating effect of 100 to 400 mK. Due to the small rise in temperature, convection and radiation effects had a negligible influence. The key lesson learnt from this simulation is that there may be sufficient contribution of heat generation solely due to bending in the rail under certain circumstances and that further work integrating into Multibody Simulation may be beneficial if other sources of heat do not make a significant contribution. From the perspective of the proposed moving vehicle rail foot flaw detection technique, the results of the initial modelling approaches are very promising for the continued development of further modelling.

Funding

Disclosure statement

The authors have no competing financial, professional, or personal interests to disclose.

References

Abidin, I. Z.; Umar, M. Z.; Yusof, M. Y.; Ibrahim, M. M.; Hamzah, A. R.; Salleh, M. N. 2012. Advantages and applications of eddy current thermography testing for comprehensive and reliable defect assessment, in *18th World Conference on Nondestructive Testing*, 16–20 April 2012, Durban, South Africa, 1–10.

Alahakoon, S.; Sun, Y. Q.; Spiryagin, M.; Cole, C. 2018. Rail flaw detection technologies for safer, reliable transportation: a review, *Journal of Dynamic Systems, Measurement, and Control* 140(2): 020801. https://doi.org/10.1115/1.4037295

ARTC. 2019. *Ultrasonic Testing By Continuous Rail Flaw Detection Vehicle*. ETE-01-02. Australian Rail Track Corporation (ARTC). Infrastructure Standards: ARTC Extranet. 12 p. Available from Internet:
https://extranet.artc.com.au/docs/eng/track-civil/procedures/rail/ETE-01-02.pdf

AS 1085.1-2002. *Railway Track Material. Part 1: Steel Rails.*

ATSB. 2015. *Derailment of freight train 6DA2 near Marryat, South Australia, on 26 July 2014*. ATSB Transport Safety Report – Rail Occurrence Investigation RO-2014-014. Australian Transport Safety Bureau (ATSB). 24 p. Available from Internet: https://www.atsb.gov.au/publications/investigation_reports/2014/rair/ro-2014-014

Bartoli, I.; Lanza di Scalea, F.; Fateh, M.; Viola, E. 2005. Modeling guided wave propagation with application to the long-range defect detection in railroad tracks, *NDT & E International* 38(5): 325–334. https://doi.org/10.1016/j.ndteint.2004.10.008

Campos-Castellanos, C.; Gharaibeh, Y.; Mudge, P.; Kappatos, V. 2011. The application of long range ultrasonic testing (LRUT) for examination of hard to access areas on railway tracks, in *5th IET Conference on Railway Condition Monitoring and Non-Destructive Testing* (*RCM 2011*), 29–30 November 2011, Derby, UK, 1–7. https://doi.org/10.1049/cp.2011.0618

Cerniglia, D.; Pantano, A.; Vento, M. A. 2012. Guided wave propagation in a plate edge and application to NDI of rail base, *Journal of Nondestructive Evaluation* 31(3): 245–252. https://doi.org/10.1007/s10921-012-0139-7

Chen, L.; Liang, Y.; Wang, K. 2010. Inspection of rail surface defect based on machine vision system, in *The 2nd International Conference on Information Science and Engineering*, 4–6 December 2010, Hangzhou, China, 3793–3796.
https://doi.org/10.1109/ICISE.2010.5691348

Christides, S.; Barr, A. D. S. 1984. One-dimensional theory of cracked Bernoulli–Euler beams, *International Journal of Mechanical Sciences* 26(11–12): 639–648.
https://doi.org/10.1016/0020-7403(84)90017-1

CI TS. 2011. *Derailment Freight Train Warracknabeal*. Rail Safety Investigation Report No 2011/07. Office of the Chief Investigator, Transport Safety (CI TS), Melbourne, Victoria, Australia. 28 p.

DelaCalle, F. J.; Garcia, D. F.; Usamentiaga, R. 2017. Inspection system for rail surfaces using differential images, in *2017 IEEE Industry Applications Society Annual Meeting*, 1–5 October 2017, Cincinnati, OH, US 1–9.
https://doi.org/10.1109/IAS.2017.8101824

Deutschl, E.; Gasser, C.; Niel, A.; Werschonig, J. 2004. Defect detection on rail surfaces by a vision based system, in *IEEE Intelligent Vehicles Symposium, 2004*, 14–17 June 2004, Parma, Italy, 507–511. https://doi.org/10.1109/IVS.2004.1336435

FLIR. 2016. *Infrared Cameras with MSX®: FLIR Ex-Series*. FLIR® Systems, Inc. Available from Internet: https://www.flir.com/instruments/ex-series

Green, R. E. 2004. Non-contact ultrasonic techniques, *Ultrasonics* 42(1–9): 9–16. https://doi.org/10.1016/j.ultras.2004.01.101

Greene, R. J.; Yates, J. R.; Patterson, E. A. 2007. Crack detection in rail using infrared methods, *Optical Engineering* 46(5): 051013. https://doi.org/10.1117/1.2738490

Grosse, C. U.; Ohtsu, M. 2008. *Acoustic Emission Testing: Basics for Research – Applications in Civil Engineering*. Springer. 406 p. https://doi.org/10.1007/978-3-540-69972-9

Hay, W. W. 1953. *Railroad Engineering*. Volume 1. Wiley. 483 p.

Hayashi, T.; Song, W.-J.; Rose, J. L. 2003. Guided wave dispersion curves for a bar with an arbitrary cross-section, a rod and rail example, *Ultrasonics* 41(3): 175–183. https://doi.org/10.1016/S0041-624X(03)00097-0

Hernandez, F. C. R.; Koch, K.; Barrera, G. P. 2007. *Rail Base Corrosion Detection and Prevention*. TCRP Web-Only Document 37. Transit Cooperative Research Program (TCRP), Transportation Research Board (TRB), Washington, DC, US. 129 p. https://doi.org/10.17226/22009

Jindal, U. C. 2012. *Strength of Materials*. Pearson India. 800 p.

Kenderian, S.; Djordjevic, B. B.; Cerniglia, D.; Garcia, G. 2006. Dynamic railroad inspection using the laser-air hybrid ultrasonic technique, *Insight – Non-Destructive Testing and Condition Monitoring* 48(6): 336–341. https://doi.org/10.1784/insi.2006.48.6.336

Kesler, K.; Zhang, Y.-J. 2007. *System and Method for Predicting Future Rail Temperature*. US20070265780A1. Available from Internet: https://patents.google.com/patent/US20070265780

Krautkrämer, J.; Krautkrämer, H. 1990. *Ultrasonic Testing of Materials*. Springer. 677 p. https://doi.org/10.1007/978-3-662-10680-8

Maldague, X. P. V. 2002. Introduction to NDT by active infrared thermography, *Materials Evaluation* 60(9): 1060–1073.

Moustakidis, S.; Kappatos, V.; Karlsson, P.; Selcuk, C.; Gan, T.-H.; Hrissagis, K. 2014. An intelligent methodology for railways monitoring using ultrasonic guided waves, *Journal of Nondestructive Evaluation* 33(4): 694–710. https://doi.org/10.1007/s10921-014-0264-6

Nippon Steel. 2019. *Rails*. Nippon Steel Corporation, Tokyo, Japan. 16 p. Available from Internet: https://www.nipponsteel.com/product/catalog_download/pdf/K003en.pdf

Michaels, D. 2014. *Understanding Rail Flaws: Identification of Common Rail Flaws*. Nordco, Inc. 97 p.

Papaelias, M. P.; Roberts, C.; Davis, C. L. 2008. A review on non-destructive evaluation of rails: state-of-the-art and future development, *Proceedings of the Institution of Mechanical Engineers, Part F: Journal of Rail and Rapid Transit* 222(4): 367–384. https://doi.org/10.1243/09544097JRRT209

Papaelias, M. P.; Lugg, M. C.; Roberts, C.; Davis, C. L. 2009. High-speed inspection of rails using ACFM techniques, *NDT & E International* 42(4): 328–335. https://doi.org/10.1016/j.ndteint.2008.12.008

Peng, D.; Jones, R. 2013. Lock-in thermographic inspection of squats on rail steel head, *Infrared Physics & Technology* 57: 89–95. https://doi.org/10.1016/j.infrared.2012.12.010

Peng, J.; Tian, G.; Wang, L.; Gao, X.; Zhang, Y.; Wang, Z. 2014. Rolling contact fatigue detection using eddy current pulsed thermography, in *2014 IEEE Far East Forum on Nondestructive Evaluation/Testing*, 20–23 June 2014, Chengdu, China, 176–180. https://doi.org/10.1109/FENDT.2014.6928257

Petcher, P. A.; Potter, M. D. G.; Dixon, S. 2014. A new electromagnetic acoustic transducer (EMAT) design for operation on rail, *NDT & E International* 65: 1–7. https://doi.org/10.1016/j.ndteint.2014.03.007

NSW Transport RailCorp. 2012. *TMC 226: Rail Defects Handbook*. Version 1.2. New South Wales (NSW) Department of Transport, Sydney, Australia. 83 p. Available from Internet: https://www.transport.nsw.gov.au/industry/asset-standards-authority/find-a-standard/rail-defects-handbook-12

Scruby, C. B.; Drain, L. E. 1990. *Laser Ultrasonics Techniques and Applications*. CRC Press. 462 p.

Sinha, J. K.; Friswell, M. I.; Edwards, S. 2002. Simplified models for the location of cracks in beam structures using measured vibration data, *Journal of Sound and Vibration* 251(1): 13–38. https://doi.org/10.1006/jsvi.2001.3978

Spiryagin, M.; Cole, C.; Sun, Y. Q.; McClanachan, M.; Spiryagin, V.; McSweeney, T. 2014. *Design and Simulation of Rail Vehicles*. CRC Press. 337 p. https://doi.org/10.1201/b17029

Tian, G. Y.; Gao, Y.; Li, K.; Wang, Y.; Gao, B.; He, Y. 2016. Eddy current pulsed thermography with different excitation configurations for metallic material and defect characterization, *Sensors* 16(6): 843. https://doi.org/10.3390/s16060843

Wilson, J.; Tian, G.; Mukriz, I.; Almond, D. 2011. PEC thermography for imaging multiple cracks from rolling contact fatigue, *NDT & E International* 44(6): 505–512. https://doi.org/10.1016/j.ndteint.2011.05.004

Yang, R.; He, Y.; Gao, B.; Tian, G. Y.; Peng, J. 2015. Lateral heat conduction based eddy current thermography for detection of parallel cracks and rail tread oblique cracks, *Measurement* 66: 54–61. https://doi.org/10.1016/j.measurement.2015.01.024

Yi, Z.; Wang, K.; Kang, L.; Zhai, G.; Wang, S. 2010. Rail flaw detection system based on electromagnetic acoustic technique, in *2010 5th IEEE Conference on Industrial Electronics and Applications*, 15–17 June 2010, Taichung, Taiwan, 211–215. https://doi.org/10.1109/ICIEA.2010.5516784

Yu, H.; Jeong, D. 2012. Railroad tie responses to directly applied rail seat loading in ballasted tracks: a computational study, in *2012 Joint Rail Conference*, 17–19 April 2012, Philadelphia, PA, US, 123–132. https://doi.org/10.1115/JRC2012-74149

Zhang, Y.-J.; Lee, S. 2008. Modeling rail temperature with real-time weather data, in *Fourth National Conference on Surface Transportation Weather; Seventh International Symposium on Snow Removal and Ice Control Technology*, 16–19 June 2008, Indianapolis, IN, US, 37–48.